arXiv:2111.08298v2 [cond-mat.soft] 1 Apr 2022

The Physics of Self-Rolling Viruses

Pedro A. Soria Ruiz[1], Falko Ziebert[1,2], and Igor M. Kulić[3,4]
[1]*Institute for Theoretical Physics, Heidelberg University, D-69120 Heidelberg, Germany*
[2]*BioQuant, Heidelberg University, D-69120 Heidelberg, Germany*
[3]*Institut Charles Sadron UPR22-CNRS, F-67034 Strasbourg, France*
[4]*Institute Theory of Polymers, Leibniz-Institute of Polymer Research, D-01069 Dresden, Germany*
(Dated: April 4, 2022)

Viruses are right at the interface of inanimate matter and life. However, recent experiments [T. Sakai, et al., J. Virol. **92**, e01522-17 (2018)] have shown that some influenza strains can actively roll on glycan-covered surfaces. In a previous letter [F. Ziebert and I. M. Kulić, Phys. Rev. Lett. **126**, 218101 (2021)] we suggested this to be a form of viral surface metabolism: a collection of spike proteins that attach to and cut the glycans act as a self-organized mechano-chemical motor. Here we study in more depth the physics of the emergent self-rolling states. We give scaling arguments how the motion arises, substantiated by a detailed analytical theory that yields the full torque-angular velocity relation of the self-organized motor. Stochastic Gillespie simulations are used to validate the theory and to quantify stochastic effects like virus detachment and reversals of its direction. Finally, we also cross-check several approximations made previously and show that the proposed mechanism is very robust. All these results point together to the statistical inevitability of viral rolling in presence of enzymatic activity.

I. INTRODUCTION

One of humanity's greatest inventions is the wheel and technological revolutions were carried by its "motorization". Being technologically so indispensable, we might ask for the wheel's utility in biology [1]. On the macroscale examples are scarce, yet in the micro realm passive rolling, e.g. of white blood cells [2] or malaria-infected red blood cells [3], occur in shear flow and are important for the functioning of the immune response and the traveling of the parasite through our body, respectively. Active self-propelled rolling was unknown for a long time. But surprisingly, the motorized wheel was rolling also in nature for ages: our old molecular adversary – the influenza virus – apparently is able to use its whole body as a chemically driven monowheel that actively rolls on our lung cells' surfaces by catalytically hydrolyzing sugars sticking out from the cell membranes. This surprising (and maybe even alarming) phenomenon of active virus surface-rolling has been demonstrated first by Sakai et al. [4, 5] and interpreted as a Brownian-ratchet-like effect. It has been also observed indirectly [6] and is discussed now as an important pathway helping the virus to cross and navigate the mucus [7, 8].

The underlying physical mechanism – different from the classical Brownian burnt bridge model [9, 10] – has been proposed recently in [11], where we outlined elements of a model which we elaborate deeper in the present work. The initial model appears to have left parts of the molecular motor community in slight disbelief [12] whether the mechanism could actually work as described. Here we explain the robustness and inevitability of the rolling state as proposed earlier and verify approximations made in [11] against more detailed analytical calculations and stochastic simulations. In addition we develop a scaling view on the mechanism. We study stochastic effects such as reversals of direction and virus detachment. And finally, we clarify how the directional stability and processivity physically emerges by pinpointing an internal "mechano-chemical flywheel" – a long-living internal polarization mode with directional memory – that allows for highly persistent rolling to occur in spite of large external noise and at zero Reynolds number.

The paper is organized as follows: in section II we describe the basic ingredients, from reaction kinetics to force balance. Section III then goes on to explain on an intuitive level why the virus actually rolls and how its rolling steady state arises. In section IV the steady rolling is studied via simple approximations allowing the force-velocity relation to be analytically investigated. Section V then describes a stochastic version of the model which we show to be consistent with the continuum version in the steady state. Beyond this limit, we also explore stochastic phenomena, like the rates of virus detachment, reversals, run lengths etc. Section VI critically scrutinizes approximations made so far and quantifies the dynamical persistence of the mechanism by studying a virus being stopped instantaneously, leading to a build-up of torque via the "flywheel" effect. Finally, in section VII we discuss implications of the model for biology/virology and we conclude with some open questions and experimental tests.

II. BASIC MODEL

We first present a mean-field description that will give much general insight into the problem and, using several approximations, allows for a detailed analytical treatment of the steady rolling.

The results derived here are formulated for any viral capsid cross-section orthogonal to the rolling direction and are equally valid for both influenza isoforms [13, 14]:

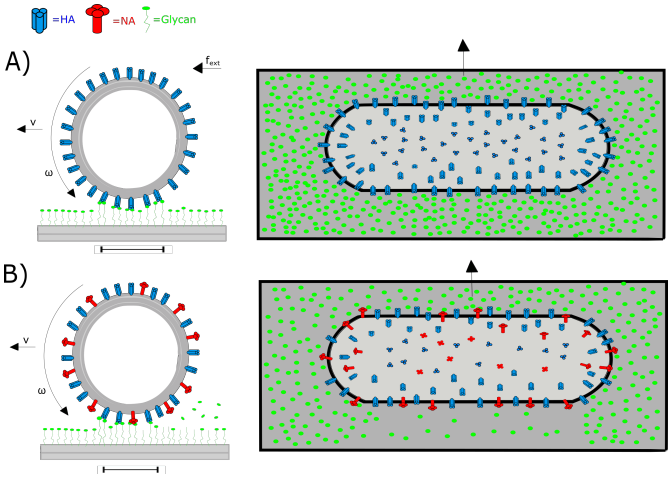


FIG. 1. Influenza A has two spike proteins on its surface: hemaglutinin (HA, blue) which attaches to sugar residues from short surface-bound glycan chains (green) and neuraminidase (NA, red) which cuts the sugar residues such that they are no longer available for HA binding. In a first step, we consider a virus rolling under an externally applied force over a glycan-covered (cf. green dots) surface, as sketched in A) as both a cross-section view and a top view. The HA-glycan binding kinetics (in the contact zone as sketched in the left panel by the bar) will result in a friction force opposing the rolling motion. B) In a second step, we consider the effect of NA cutting. The dynamic self-organization (self-polarization) of the bound linker profile in the contact zone now allows for steady self-rolling. The NA "consumes" glycans which leads to a depleted trail on the back of the virus (see right panel).

the cylindrical (filamentous) and the spherical virus geometry. The main difference between the two cases is the system size (total number of interacting spike proteins) and the enhanced role of fluctuations for spherical or smaller aspect ratio viruses. Stochastic effects are postponed to section V, where we also critically scrutinize the validity of the assumptions made here.

A. Influenza spike proteins and their kinetics

As one of the omnipresent molecular adversaries of mankind, the influenza virus (IV) and its proteins have been extensively characterized [15–18]. As often in the virus realm, influenza is in fact a whole family of viruses that have evolved slightly differently. We will focus here on the two viruses where motility has been evidenced experimentally [4, 5], namely influenza-A (IVA) and influenza-C (IVC).

IVA has two spike proteins that interact with the host membrane: Hemaglutinin (HA) and Neuraminidase (NA), see Fig. 1. These are distinct $\sim 10\,\mathrm{nm}$ sized entities (HA is a trimer, NA a tetramer) that perform two distinct and mutually competing functions: HA binds to sialic acid residues of glyco-peptides and lipids coating the surface of our cells, while NA acts antagonistically by hydrolytically cutting the same sialic acid residue that HA binds to. Importantly, for steric reasons the residue can be either bound by one HA or by one NA molecule, but not by both at the same moment. In IVC, the two proteins are fused together into a single spike protein [19], meaning the "attaching spike" and the "cutting spike" are co-localized. But again, only one of the binding sites can interact with a glycan residue at a time. Note that this renders IVA more flexible, as it can for instance polarize its HA-NA distribution on its surface and engage in other mechanisms of motion than described here, as discussed previously [20]. This motion however is a much slower process, cf. section VII. Due to lack of available experimental data, we study here the kinetics with IVA parameters and assume that the values for IVC (once available) should be of similar order.

The binding/unbinding kinetics of HA will be described via on/off rates k_{on}, k_{off}. These have been characterized experimentally [21, 22] yielding a dissociation constant $K_d = \frac{k_{off}}{k_{on}} = 1\text{-}5\,(\text{we use } 2)\ \mathrm{mM}$, $k_{off} = 10^{-1}\text{-}1\,(1)\,\mathrm{s}^{-1}$ and $k_{on} = 0.01\text{-}1\,(0.5)\,\mathrm{mM}^{-1}\mathrm{s}^{-1}$. NA transiently binds (with rates k_1, k_{-1}) and then enzymatically cuts the sialic residues with a rate k_{cut}, making the glycans irreversibly inactive for HA binding. We hence use a Michaelis Menten description with a Michaelis constant $K_M = (k_{-1} + k_{cut})/k_1$. NA's enzymatic activity has also been measured [23] to yield $K_M \simeq 14.3\ \mathrm{mM}$ and $k_{cut} \simeq 15\,\mathrm{s}^{-1}$, implying $V_{cut} = k_{cut} N_{NA} = 15\,\mathrm{mMs}^{-1}$ for a typical NA concentration of $N_{NA} = 1\ \mathrm{mM}$.

B. Contact interval

During virus rolling all the force generation happens in the virus-substrate contact region, i.e. the interface where the virus and the glycan-coated substrate (cell membrane) meet. Here we roughly estimate the size of this region for a cross-section of a cylindrical (or spherical) virus and will later substantiate the result by considering the full binding kinetics, cf. section VI A.

We assume that glycan chains are present at a high concentration G_0 – well in excess to spike proteins (throughout this work we use $G_0 = 10\,\mathrm{mM}$ and for the HA spike concentration $H_0 = 2\,\mathrm{mM}$, as estimated earlier [11]). The glycan chains are constantly binding to and unbinding from the HA spike proteins and elongate to a length $l = R(1 - \cos\phi)$ in that process, where ϕ is the angle measured from the virus symmetry axis and R the virus radius. If bound they gain a free energy

$$\Delta G = k_B T \ln\left(\frac{G_0}{K_d}\right) \tag{1}$$

with K_d the dissociation constant. In turn they have to pay the elastic energy of getting stretched

$$E_{el}(\phi) = \frac{S}{2} l^2 \simeq \frac{SR^2}{8}\phi^4 \ \text{ for } \ \phi \ll 1, \tag{2}$$

where glycan chains were considered ideal linear springs with spring constant $S \sim 0.01\text{-}1\, k_B T/\mathrm{nm}^2$ - a typical range for polymers of few nm length (we chose $0.1 k_B T/nm^2$). Note that the cylindrical (or spherical) geometry of the virus results in a strong dependence on the angle ϕ and on the virus radius R (which for IV is typically $\simeq 50$ nm). We neglect here the effect of NA binding for simplicity, since it is short lived compared to HA.

Balancing the two energy terms yields the typical angular size of the contact zone with $\phi \in [-\phi_c, \phi_c]$ to be

$$\phi_c = \left(\ln\left(\frac{G_0}{K_d}\right) \frac{8kT}{SR^2} \right)^{1/4}. \tag{3}$$

In the following we assume the contact area size to be a constant, even when the virus is rolling.

C. Torque balance

The torque of an attached virus can be calculated using the stretching force per linker $F_{el} = -\frac{\partial}{\partial l} E_{el}$ yielding a torque $\propto SR^2 (1-\cos\phi)\sin\phi \simeq \frac{1}{2} SR^2 \phi^3$ for small angles. If the linkers have an angular density $\rho_{HA}\, b(\phi)$ with ρ_{HA} the angular density of HA spikes and $b(\phi)$ the angular probability density of each linker being bound, the total torque acting on the virus is just the integral over all bound linkers,

$$m = -m_0 \int_{-\phi_c}^{+\phi_c} b(\phi)\, \phi^3 d\phi, \tag{4}$$

with $m_0 = \frac{1}{2} SR^2 \rho_{HA}$ the characteristic torque scale.

When the virus is rolling at typical angular speeds, experimentally $\omega \simeq 1\,\mathrm{s}^{-1}$ [5], using typical densities of linkers one can estimate all other torques, e.g. from hydrodynamics, to be negligible. Therefore the torque balance $m = 0$ has to hold (to very good approximation) at all times.

Note that for simplicity we assumed here that there is no compression of the chains by the virus – except at $\phi = 0$ to fulfill force-balance. This simplification can be relaxed as explained in appendix B.

D. Dynamics of bound linkers and free glycans

The binding of the HA spikes to the glycans can be described by a simple on-off kinetics. Denoting the bound HA-glycan linker concentration by B, the unbound (open) HA concentration by O and the free glycans by G, one has $\partial_t B = k_{on} G\, O - k_{off} B$ and an equation with opposite signs on the r.h.s. for $\partial_t O$. Obviously, as $O + B = H_0$ with H_0 the total number of HA, one can immediately eliminate the equation for the open HA.

Adding the dynamics for the free glycans, one can write

$$\partial_t B + \omega \partial_\phi B = \quad k_{on} G (H_0 - B) - k_{off} B\,, \tag{5}$$

$$\partial_t G + \omega \partial_\phi G = -k_{on} G (H_0 - B) + k_{off} B - f_{cut}\,, \tag{6}$$

were we accounted for a (potential) rolling with angular velocity ω, leading to advection of all concentration profiles as reflected by the second term on the l.h.s., and for the enzymatic cutting of G by the NA spikes as reflected by the total cutting rate f_{cut} acting as a sink.

It is important to note that we made the approximation that the on/off-kinetics of HA-glycan binding satisfies $\frac{k_{off}}{k_{on}} = K_d$. That is, we neglected that K_d is in general stretching force- [24] and hence angle-dependent. This – rather violent-looking – approximation allows for an analytical treatment. After having understood the general mechanism of virus rolling, we show in section VI A that the angle-dependence can be included – in both continuum numerics and stochastic simulations – and that this proper account of the detailed balance does not change the behavior qualitatively. In other words, at this stage, in the simple model we use the stretch-dependence only to determine the size of the contact interval, but not for the kinetics. Hence the glycan-binding profile of a static virus will be box-like (constant in the contact interval and zero outside) while in reality it decays with $\exp(-\phi^4)$, cf. section VI A.

The total cutting rate f_{cut} can be approximated by a Michaelis-Menten kinetics, as discussed in section II A, with a Michaelis constant K_M and a cutting velocity of the sialic acid (glycan) residues, $V_{cut} = k_{cut} N_{NA}$ set by the enzymatic turnover rate k_{cut} and the enzyme concentration N_{NA}, giving $f_{cut} = \frac{V_{cut} G}{K_\mathrm{M} + G}$.

Finally, the minimal model reads

$$\partial_t B + \omega \partial_\phi B = k_{on} G (H_0 - B) - k_{off} B, \tag{7}$$

$$\partial_t G + \omega \partial_\phi G = -k_{on} G (H_0 - B) + k_{off} B - \frac{V_{cut} G}{K_\mathrm{M} + G} \tag{8}$$

and has to be solved on the contact interval $\phi \in [-\phi_c, \phi_c]$ with ϕ_c given by Eq. (3) and together with the torque balance constraint, i.e. m defined in Eq. (4) must be zero at all times.

III. STEADY ROLLING - SCALING AND NUMERICS

Let us now discuss the just proposed – deterministic and mean field-type – model in the steady state on the scaling level. In steady state, the virus is either not moving at all or rolls with constant angular velocity ω. The first main question is: are states with $\omega \neq 0$ possible and if so to understand and analyze the causing mechanism.

A. Scaling arguments

Before diving into the detailed calculations, let us try to explain the rolling motion using simple scaling arguments. Our focus lies on what the bound linker distribution looks like in the contact zone and the effects thereof for the torque balance.

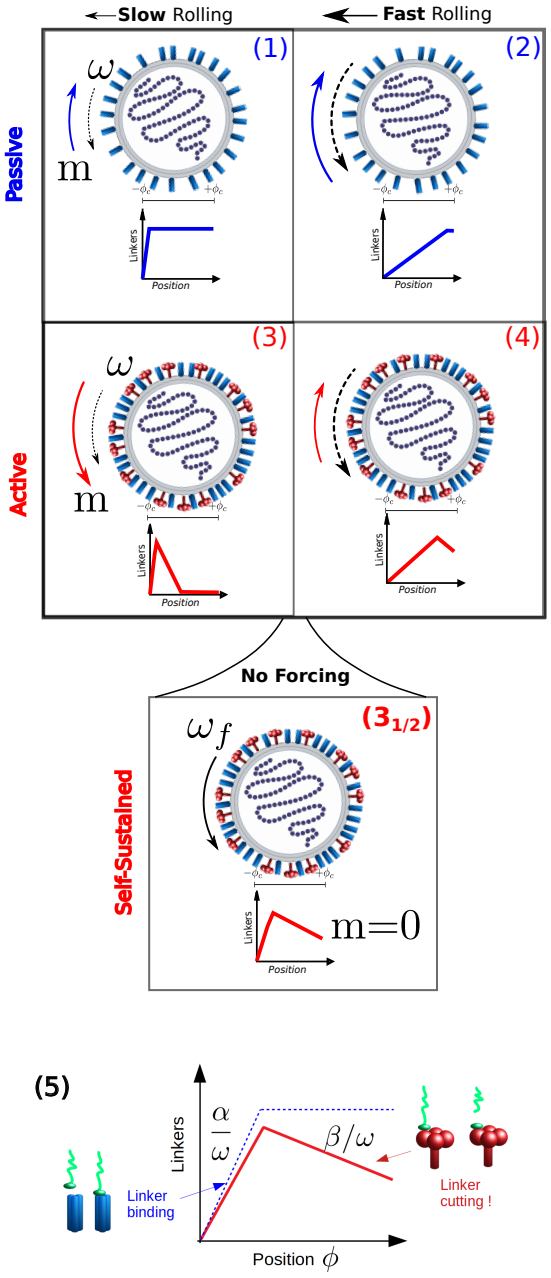


FIG. 2. Sketches of rolling virus cross-sections with representations of their bound linker distributions within the contact zone. Panels (1), (2): passive case (no NA activity) for low vs. high angular velocity ω. Here the rolling must be due to an externally applied force and the linker-induced torque, m, counteracts the rotation. Panels (3), (4): active case with enzymatic NA activity, again for low and high ω. The linker-induced torque accelerates (3) or decelerates (4) the rotation. Panel ($3_{1/2}$): steady state, where the two regions at the front and back counteract and the total torque is zero. (5) Zoom of the passive (blue dashed) and active (red) profiles with characteristic profile slopes α and β (see text)

First consider the simplest case of a virus that is forced to roll by an externally applied torque – as sketched in Fig. 1A) – and that does not have enzymatic NA activity, i.e. only binds its HA to the glycans on the surface. In rolling direction, the virus encounters unbound glycans and the HA needs time to bind, which means the bound HA-glycan distribution in the co-moving virus frame has the shape as sketched in Fig.2(1): it increases from zero with a certain slope and levels off at a plateau value B_{pl}, corresponding to the mean bound linker distribution a non-moving virus would have. The slope is determined by two quantities: first, the linker attachment rate

$$\alpha = k_{on} H_0 G_0 \tag{9}$$

which is linked to the plateau value by $\alpha t_{pl} = B_{pl}$, with t_{pl} the time it takes to establish the equilibrium plateau. The second is the actual rolling speed of the virus ω. Since $\omega t \sim \phi$ the slope in the angular distribution $B(\phi)$ is in fact given by $\frac{\alpha}{\omega}$. Consequently, one expects the slope to be steep for a slowly rolling virus and shallow if the virus rolls very fast, cf. Fig. 2(1) vs. (2).

Now let us add a weak enzymatic cutting by NA. In rolling direction, the binding kinetics will still dominate, for weak NA cutting rate ω. Hence the binding-induced positive slope in the attachment-region prevails. For a steady rolling virus, however, with the distance from the front, the NA has linearly more time to cut off the glycans and hence one expects that the second, plateau region is transformed into an approximately linear, negative slope which we denote by β. This slope has in general a complicated parameter dependence, but it will be roughly proportional to the enzymatic cutting velocity

$$\beta \propto V_{cut}. \tag{10}$$

By the same argument as before, the slope in the angular distribution $B(\phi)$ is given by $\frac{\beta}{\omega}$ and the slope at the back is steep for a slowly and shallower for a rapidly rolling virus, cf. Fig. 2(3) vs. (4). Fig. 2(5) shows a zoom on the contact zone with the slopes labeled and with sketches of their different origins.

What are the consequences of these linker distributions for the overall torque? Note that a homogeneous, constant distribution $B(\phi)$ (and likewise any symmetric one) is perfectly balanced. Hence the linkers always missing at the front due to the time it needs to establish the equilibrium distribution imply that there is an excess force acting on the back, resulting in a torque counteracting the rotation, as indicated e.g. in Fig. 2(1) where the torque m is acting against ω. Consequently, the attachment dynamics results in an effective friction. In turn, the second, negative slope implies the opposite: an excess force on the front, accelerating the motion. Note that this is not forbidden thermodynamically: the action of NA is an active process consuming, or rather cutting in an irreversible manner, the glycans. Now it depends on the relative slopes/relative sizes of the two regions whether the virus is overall accelerating, as in Fig. 2 (3),

or decelerating as in Fig. 2 (4). In between there is the possibility of a stationary state where the overal torque is zero, as sketched in Fig. 2($3_{1/2}$). This exactly corresponds to the searched-for steady rolling state in the absence of external driving.

We can substantiate this argument by estimating the torque-angular velocity relation. This relation is a *nonlinear* function – and hence allows for non-trivial steady states – due to the different ω-dependencies of the two regions, the attachment-dominated front and the cutting-dominated back. In fact, for the attachment dynamics, if the respective region is small, the torque evaluates to $m_{att} \propto -\frac{\alpha}{\omega} \cdot \phi_{pl}^2 \cdot \phi_c^3$, where the first term is the profile's slope, the second term arises from the integral over the linear slope up to ϕ_{pl}, the angle where the plateau begins, and ϕ_c^3 is related to the geometric lever arm. The minus sign indicates the direction, opposed to the rotation. Since $\phi_{pl} = \omega t_{pl}$ one gets $m_{att} \propto -\phi_c^3 \, \alpha \, \omega$, i.e. a "Stokesian hydrodynamics"-like friction linear in ω. In contrast, for the cutting dynamics the contribution of the small front region does not matter as cutting takes place everywhere at a uniform rate. Hence the torque integral over the region of cutting is $m_{cut} \propto \frac{\beta}{\omega} \cdot \phi_c^2 \cdot \phi_c^3$, i.e. depends on ω only via the slope. The positive sign indicates its accelerating effect discussed above. Clearly, the overall torque balance $0 = m = m_{att} + m_{cut}$, allows for steady state solutions of the type

$$\omega \propto \pm \phi_c \sqrt{\frac{\beta}{\alpha}} \propto \sqrt{V_{cut}}. \tag{11}$$

That is, the steady state rolling velocity grows rapidly for small cutting velocities V_{cut}.

B. Time-angle correspondence and numerical solution

Let us confirm numerically that self-rolling is possible. In the steady state we can drop the time derivative in Eqs. (7), (8) and have to solve

$$\omega \partial_\phi B = k_{on} G \, (H_0 - B) - k_{off} B \tag{12}$$

$$\omega \partial_\phi G = -k_{on} G \, (H_0 - B) + k_{off} B - \frac{V_{cut} G}{K_\mathrm{M} + G}, \tag{13}$$

combined with $b(\phi) = B(\phi)/H_0$ giving the closure condition in terms of the torque balance, Eq. (4)

$$m = -\frac{m_0}{H_0} \int_{-\phi_c}^{+\phi_c} B\,(\phi)\, \phi^3 d\phi = 0\,. \tag{14}$$

To do so, we can apply the following strategy, which could be called "time-rotation angle correspondence". The angular advection operator, $\omega \partial_\phi$, and the time derivative operator, ∂_t, can be treated on the same grounds by replacing time with the angle scaled by the angular frequency: $t \to \frac{\phi + \phi_c}{\omega}$ (or $\phi = \omega t - \phi_c$). The time window corresponding to passing the contact interval $[-\phi_c, \phi_c]$ is then $[0, T]$ with $T = \frac{2\phi_c}{\omega}$.

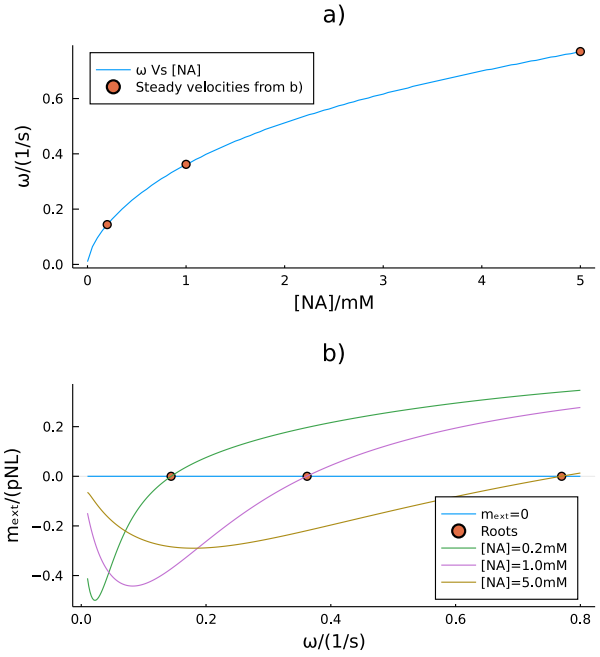


FIG. 3. a) Angular velocity ω of the steady rolling state as a function of NA concentration $N_{NA} = [NA]$. One abtains a square-root behavior, $\omega \propto \sqrt{N_{NA}}$, as suggested by scaling. b) Adding an external torque m_{ext} allows to obtain the torque-angular velocity relation, which is a nonlinear function of ω. Three different values of NA concentration are shown, the respective free rolling velocities (for $m_{ext} = 0$) are also indicated in a).

This observation suggests to think of the steady state as a dynamic relaxation of the concentrations on the time interval $[0, T]$. One can hence treat the problem as an initial value problem at one boundary of the interval (the one in rolling direction) with $B\,(0) = 0$ and $G\,(0) = G_0$ (in the not yet visited region, nothing has bound and no glycan has been consumed yet): the solution of the dynamic problem $B_{dyn}\,(t)$ on a time interval $[0, T_{test}]$ can be obtained without any reference to the actual angular frequency ω.

In a second step $B_{dyn}\,(t)$ can be used to obtain the torque by evaluating

$$m = -\frac{m_0}{H_0} \int_0^{t_{up}=2\phi_c/\omega} B_{dyn}\,(t)\,(\omega t - \phi_c)^3\, \omega dt \tag{15}$$

Note that high frequencies correspond to taking the integral over a short time interval and vice versa. Given the curve $B_{dyn}\,(t)$ on a large enough interval, $[0, T_{test}]$ with $T_{test} > T$ for all considered ω values, one can now scan the upper boundary $t_{up} = 2\phi_c/\omega$ by varying the angular frequency and hence determine ω such that $m\,(\omega) = 0$, which is a simple root finding problem. Solving along the same lines for $m\,(\omega) = m_{ext}$, with an external torque m_{ext}, allows also to obtain the torque-angular velocity relation.

Fig. 3 a) shows the angular velocity of the steady rolling state, obtained numerically, as a function of enzymatic activity, i.e. NA concentration. One clearly sees the square-root behavior as obtained by scaling, $\omega \propto \sqrt{\beta}$ with $\beta \propto V_{cut} \propto N_{NA}$. Fig. 3 b) shows the torque-angular velocity relation obtained numerically for three values of NA concentration. Free rolling corresponds to $m_{ext} = 0$.

The results obtained numerically and shown in Fig. 3 are intriguing: in fact, any – even a small – enzyme activity leads to finite rolling motion in this mean field-type model. The response of the motor close to free rolling is as expected – an assisting torque speeds up the rolling and a counter torque slows it down, but there is a strong nonlinear dependence for higher counter torques. Both these findings can be understood analytically and can be related to the parameters of the spike dynamics, as shown in the next section. They will then be critically compared to a model including stochastic fluctuations in section V.

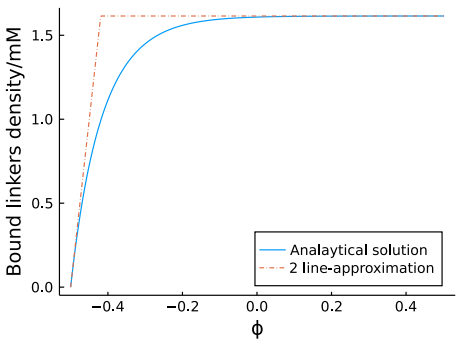


FIG. 4. The blue curve shows the bound linker profile on the contact angle interval $[-\phi_c, \phi_c]$ as given by Eq. (17). The virus is forced to roll to the left. The fact that the linkers need time to bind to the newly encountered substrate is reflected by the increase on the left leveling to a plateau, cf. Fig. 2 and the discussion is section III A. The dashed lines show the two-line approximation given by Eq. (22). Parameters as given in section II, implying $\phi_c \simeq 0.5$.

IV. STEADY ROLLING - ANALYTICAL THEORY

In the steady state much analytical insight can be gained using the main ideas introduced in the last chapter, i.e. the time-angle-correspondance and the "line-approximations" of the linker profiles, as sketched in Fig. 2.

A. Analytical solution for forced rolling without enzymatic activity

We first consider the passive case, i.e. in absence of catalytic activity. That is, we assume that the virus is forced to roll with a given steady-state angular velocity ω by a weak, externally applied torque. For $V_{cut} = 0$ and in the steady state, Eqs. (12, 13) imply the conservation law $\partial_\phi (B + G) = 0$. Assuming a homogeneous initial glycan coverage G_0, we can hence rewrite $G(\phi) = G_0 - B(\phi)$. This reduces the problem to a single equation

$$\omega \partial_\phi B = k_{on} (G_0 - B) (H_0 - B) - k_{off} B \tag{16}$$

which, for the initial condition $B(-\phi_c) = 0$ (rolling to the left), can be solved exactly

$$B(\phi) = \frac{C_0 - C_1}{2} - \frac{C_1}{\frac{C_0+C_1}{C_0-C_1} e^{\frac{C_1 k_{on}}{\omega}(\phi+\phi_c)} - 1}. \tag{17}$$

Here $C_0 = H_0 + G_0 + K_d$, $C_1 = \sqrt{C_0^2 - 4H_0G_0}$ are constants determined by the concentrations and reaction kinetics. The solution can also be given in time-domain:

$$B(t) = \frac{C_0 - C_1}{2} - \frac{C_1}{\frac{C_0+C_1}{C_0-C_1} e^{C_1 k_{on} t} - 1}. \tag{18}$$

The resulting bound linker profile on the contact angle interval $[-\phi_c, \phi_c]$ is shown in Fig. 4, cf. also the cases sketched as (1) and (2) in Fig. 2. It is characterized by an increase of the bound HA-glycan links leveling at a plateau value of

$$B_{pl} = \frac{C_0 - C_1}{2}. \tag{19}$$

For simplicity, and to be able to proceed with a perturbative approach taking enzymatic activity into account, we approximate the exact profile by two lines: first, in the region of its rapid increase, B is approximated by the slope at the front, and in the second region by its plateau value. This is most transparent in time-space where one has

$$B(t) = \begin{cases} \alpha t & \text{for } 0 \le t \le t_m \\ \alpha t_m & \text{for } t_m \le t \le T \end{cases} \tag{20}$$

for $t \in [0, T]$ with $T = \frac{2\phi_c}{\omega}$ as before and

$$\alpha = k_{on} H_0 G_0 \,, \quad t_m = \frac{B_{pl}}{\alpha} \tag{21}$$

with α the initial slope (i.e. the linker binding velocity) and t_m the time needed to reach the plateau/maximum (cf. t_{pl} discussed in section III A). In angle-space one has

$$B(\phi) = \begin{cases} \frac{\alpha}{\omega}(\phi + \phi_c) & \text{for } \phi \in [-\phi_c, \phi_{pl}] \\ \frac{\alpha}{\omega}(\phi_{pl} + \phi_c) = B_{pl} & \text{for } \phi \in [\phi_{pl}, \phi_c] \end{cases} \tag{22}$$

with ϕ_{pl} the angle where the plateau is reached. This angle space view is especially transparent to derive the scaling discussed earlier, cf. appendix A.

B. Multiple-line approximations

One can proceed the analysis by using the approximations of the bound linker profiles by several lines. Typically, two lines are needed, cf. the cases sketched in Fig. 2 as (1),(2),(4). When the linkers are completely cut at the back, three lines are needed, cf. Fig. 2 (3). These multiple-line approximations also allow us to treat the effect of enzymatic activity analytically and to discuss the generic physics of the torque-angular velocity relation associated with a given bound linker profile.

1. Case of no enzymatic activity

This is the case just discussed where $B(t)$ is approximately given by Eq. (20). The clear advantage of a line approximation is that we can calculate the torque integral analytically. From Eq. (4) we have to evaluate

$$m = -\frac{m_0\omega^4}{H_0}\int_0^T \left(t-\frac{T}{2}\right)^3 B\left(t\right) dt \tag{23}$$

with $T=\frac{2\phi_c}{\omega}$. Importantlly, we can write this as an integral of the constant plateau value over the full range, $\propto \int_0^T \left(t-\frac{T}{2}\right)^3 B_{pl}\, dt = 0$, which vanishes due to symmetry, plus an integral over the first zone only (the one at the front in rolling direction)

$$m = -\frac{m_0\omega^4}{H_0}\int_0^{t_m} \left(t-\frac{T}{2}\right)^3 \alpha(t-t_m) dt\,. \tag{24}$$

This highlights the fact that the torque arises from the imbalance/asymmetry of the linker distribution associated with linkers having to form in rolling direction in the region $0 \le t \le t_m$.

Before solving in full generality, we can assume that the plateau is rapidly reached, i.e. $t_m \ll T$, yielding

$$m \simeq \frac{m_0\omega^4}{H_0}\alpha\left(\frac{T}{2}\right)^3\int_0^{t_m}(t-t_m)dt = -\frac{m_0}{H_0}\frac{\phi_c^3}{2}\frac{B_{pl}^2}{\alpha}\omega, \tag{25}$$

where we used $T=\frac{2\phi_c}{\omega}$ and $t_m = B_{pl}/\alpha$. Eq. (24) can also be integrated completely to yield

$$m = \frac{m_0}{H_0}\frac{\alpha}{80}\omega^4 T^5 p\left(\frac{t_m}{T}\right) \tag{26}$$

with the polynomial

$$p\left(x\right) = -x^2\left(5-10\,x+10\,x^2-4\,x^3\right) \tag{27}$$

for $t_m \le T$; for $t_m > T$ one has to use $p(1)=-1$.

Let us discuss the limits. For very slow rolling, cf. Fig. 2(1), the first, attachment-dominated regime shrinks with only the plateau left, and the torque hence vanishes due to symmetry. For $t_m \ll T$, corresponding to intermediate rolling speeds and sufficiently rapid build-up of the plateau, one has $p(x) \simeq -5x^2$ which agrees with Eq. (25). Hence for intermediate rolling speed one gets for the torque-velocity relation for passive rolling,

$$m_{diss}\left(\omega\right) = -\xi_{diss}\omega\ ,\quad \xi_{diss} = \frac{m_0}{H_0}\frac{\phi_c^3}{2}\frac{B_{pl}^2}{\alpha}. \tag{28}$$

This is a purely frictional torque, acting against the motion and linear in ω. The effective friction constant, ξ_{diss}, is determined by both the slope, α, and the plateau value, B_{pl}, of the bound linker distribution, as well as the size of the contact interval ϕ_c, which themselves contain all system parameters.

For faster rolling, the friction is determined by $p(x)$. For very fast rolling, faster even than in Fig. 2(2), the linking is so slow compared to the rolling that there will be no plateau at all. In that case, one evaluates $m = -\frac{m_0}{H_0}\alpha\omega^4 T^5\frac{1}{80}$, which corresponds to the value $p(1)$. The torque is hence still frictional and due to $T=\frac{2\phi_c}{\omega}$ scales with ω^{-1}. Hence in this regime, the faster the rolling the less friction: less linkers bind because of limited time and hence fewer resist the motion. Overall, friction first increases, then is given by $p(x)$ and then decreases again.

2. Case of weak enzymatic activity

In the presence of enzymatic NA activity, cf. Fig. 2(3)-(5), the first region of increasing linker density is still present (in fact, only slightly modified), while the plateau is transformed into a slowly decreasing function, implying $B(t)$ having a maximum around t_m. Focusing on cases (4),(5) where the glycan is not completely cut at the back, we can use the following parameterization

$$B\left(t\right) = \begin{cases} \alpha t & \text{for } 0 \le t \le t_m \\ \alpha t_m - \beta\left(t-t_m\right) & \text{for } t_m \le t \le T \end{cases} \tag{29}$$

with two non-negative constants $\alpha > 0, \beta \ge 0$ (with $\beta = 0$ corresponding to the case without NA activity just discussed, without maximum but a plateau). At the moment β is just a parameter. In section IV C we will determine it as a function of the underlying model parameters using perturbation theory.

We can again bring the torque integral in a convenient form (using that the integral over the plateau over the full contact area vanishes) and get

$$m = -\frac{m_0\omega^4}{H_0}\left[\int_0^{t_m}\alpha(t-t_m)\left(t-\frac{T}{2}\right)^3 dt - \int_{t_m}^{T}\beta(t-t_m)\left(t-\frac{T}{2}\right)^3 dt\right] \tag{30}$$

If the plateau is rapidly reached, $t_m \ll T$, one obtains

$$m = -\frac{m_0}{H_0}\left[\alpha\omega\frac{1}{2}\left(t_m\right)^2\phi_c^3 - \frac{\beta}{\omega}\frac{2}{5}\phi_c^5\right]. \tag{31}$$

(this is also derived in Eq. (A4)). Importantly, the second term has the opposite sign – it is active – since now

$t > t_m$ in the integration. Secondly, the second term is independent of t_m for small t_m, which leads to the $1/\omega$ dependence.

Eq. (30) can again be integrated completely, yielding

$$m = \frac{m_0\omega^4}{H_0}T^5\left\{\frac{\alpha}{80}\,p\left(\frac{t_m}{T}\right)+\frac{\beta}{80}\left[p\left(\frac{t_m}{T}\right)+1\right]\right\}. \tag{32}$$

We hence get the relation

$$\frac{80H_0}{(\alpha+\beta)\,\omega^4T^5}\frac{m}{m_0} = p\left(\frac{t_m}{T}\right)+\frac{\beta}{\alpha+\beta}, \tag{33}$$

from which one can draw general conclusions: First, $\omega = 0$, implying $T = \infty$ and hence $\frac{t_m}{T} = 0$ and $p\left(\frac{t_m}{T}\right) = 0$, is a solution for $\beta = 0$. This corresponds to the static, non-rolling case without activity. Next, the polynomial $p\left(\frac{t_m}{T}\right)$ is always negative (except for $\frac{t_m}{T} = 0$), with its modulus increasing with t_m. Therefore, only when the term $\beta > 0$ is present, there is the possibility to ensure $m \propto p\left(\frac{t_m}{T}\right)+\frac{\beta}{\alpha+\beta} = 0$, i.e. torque balance, for finite $\frac{t_m}{T}$ and hence ω. On the other hand, for any $\beta > 0$ there is in fact always a solution $t_m = t_m^*$ at which the torque vanishes, namely

$$p\left(\frac{t_m^*}{T}\right) = -\frac{\beta}{\alpha+\beta}.$$

We have hence shown that, at least in two-slope approximation, *any finite enzyme activity will induce motion* in the simple model.

3. Case of slow rolling and high enzymatic activity: three-line approximation

Let us discuss the case sketched in Fig. 2(3). So far we had assumed that the bound linkers cannot decay to zero in the time interval $[0, T]$. However, for small ω and high β, the two-line approximation breaks down if the bound linker concentration becomes negative in $[t_0, T]$ with $\alpha t_m - \beta\,(t_0 - t_m) = 0$ or

$$t_0 = \frac{\alpha+\beta}{\beta}t_m. \tag{34}$$

To cover the whole range of frequencies, we generalize the profile to a Three-Line-Approximation (3LA) by writing

$$B\,(t) = \begin{cases} \alpha t & \text{for } 0 \le t \le t_m \\ \alpha t_m - \beta\,(t - t_m) & \text{for } t_m \le t \le t_0 \\ 0 & \text{for } t_0 \le t \le T \end{cases} \tag{35}$$

We simplify the evaluation of the torque integral as follows: in the limit of small ω (i.e. large T) and not too high β (such that $t_0 > t_m$ and $\frac{\alpha+\beta}{\beta} \simeq \frac{\alpha}{\beta}$) the integral over the second region dominates over the first, which is very small (rapid rise to the plateau), and the third region does not contribute anyways. It is hence enough to evaluate

$$m \simeq -\frac{m_0\omega^4}{H_0}\int_{t_m}^{t_0}\left(t-\frac{T}{2}\right)^3(\alpha t_m - \beta\,(t-t_m))\;dt$$

Moving the lower boundary to 0 and using $t_0 \simeq \frac{\alpha}{\beta}t_m$ (as discussed above) one gets by neglecting terms which are a factor t_m/t_0 smaller

$$m \simeq -\frac{m_0\omega^4}{H_0}\frac{\beta}{80}T^5p\left(\frac{t_0}{T}\right) \tag{36}$$

with still the same polynomial, cf. Eq. (27).

4. Full torque-angular velocity relation

Using $T = \frac{2\phi_c}{\omega}$ one can introduce the characteristic frequency

$$\omega_0 = \frac{2\phi_c}{t_0} = \frac{2\phi_c}{t_m}\frac{\beta}{\alpha} \tag{37}$$

to replace the argument of the polynomial in Eq. (36) by ω/ω_0. Rescaling as $\tilde{\omega} = \omega/\omega_0$ one gets the following torque-angular velocity relation for small frequencies, $\tilde{\omega} < 1$, i.e. $\omega < \omega_0$:

$$m = m_0\frac{B_{pl}}{H_0}\frac{\phi_c^4}{5}\tilde{\omega}\cdot\left(-4\,\tilde{\omega}^3+10\,\tilde{\omega}^2-10\,\tilde{\omega}+5\right). \tag{38}$$

For larger frequencies , $\tilde{\omega} > 1$, we can use Eq. (31), which can be rescaled the same way to yield

$$m = -m_0\frac{B_{pl}}{H_0}\frac{\phi_c^4}{5}\left(5\frac{\beta}{\alpha}\tilde{\omega}-\frac{1}{\tilde{\omega}}\right). \tag{39}$$

We hence have established the full torque-angular velocity relation for a rolling virus. While α is determined simply by the HA-glycan on-kinetics, β is yet not specified. We will determine it in the next section by a perturbation expansion of the non-enzymatic state and postpone the discussion of the steady rolling and the torque-angular velocity relation to section IV D.

C. Including enzymatic activity: perturbative solution

We now include the enzymatic activity of NA and treat it as a perturbation of the forced-rolling steady state, obtained in section IV A, where HA-glycan binding leads to the two-line profile with a rapid increase at the front (characterized by α) leveling off to a plateau.

We hence assume that $\epsilon = V_{cut}/\alpha$ is a small parameter i.e. the enzyme cutting activity is small against the binding kinetics. We then can write

$$B = B_1 + \epsilon B_2 + \dots\,,\; G = G_1 + \epsilon G_2 + \dots. \tag{40}$$

such that the zero order $\mathcal{O}(\epsilon^0)$ is just the passive (i.e. forced rolling) case of section IV A.

To next order $\mathcal{O}(\epsilon)$ one has to consider

$$\begin{aligned}\omega B_2' &= k_{on}H_0G_2 - k_{off}B_2 - k_{on}\left(G_1B_2 + B_1G_2\right),\\ \omega G_2' &= -k_{on}H_0G_2 + k_{off}B_2 + k_{on}\left(G_1B_2 + B_1G_2\right)\\ &\quad -\frac{k_{on}H_0G_0G_1}{K_M+G_1}.\end{aligned} \tag{41}$$

As the binding kinetics is assumed to be fast, we use an adiabatic approximation, $\omega B_2' \simeq 0$. Then the equations for G_2 and B_2 simplify to

$$\omega G_2' = -\frac{k_{on}H_0G_0G_1}{K_M+G_1}\,,\;\; B_2 = \frac{H_0-B_1}{K_d+G_1}G_2\,. \tag{42}$$

Neglecting the boundary layer close to the front, we can replace $B_1 \simeq B_{pl}$, $G_1 \simeq G_{pl} = G_0 - B_{pl}$ by their plateau values. Also note that $G_2(t=0) = 0$, since the boundary conditions at the front are already fulfilled in zero order. Transforming to time space we get the dynamical profile for the glycans $G_2(t) = -\frac{k_{on}H_0G_0G_{pl}}{K_M+G_{pl}}t$ and hence for the bound linkers

$$B_2(t) = -\frac{H_0-B_{pl}}{K_d+G_{pl}}\frac{k_{on}H_0G_0G_{pl}}{K_M+G_{pl}}t\,. \tag{43}$$

Transforming back to angle space and using $\epsilon = V_{cut}/\alpha$ where $\alpha = k_{on}H_0G_0$, yields [25] $B_2 = -\alpha f\,\frac{\phi+\phi_c}{\omega}$ or

$$\beta = V_{cut}f\,,\;\; f = \frac{H_0-B_{pl}}{K_d+G_{pl}}\frac{G_{pl}}{K_M+G_{pl}}. \tag{44}$$

This result directly implies an expansion for the torque,

$$m = m_1 + \epsilon m_2, \tag{45}$$

where $m_1 = m_{diss}$ is the passive torque, given in Eq. (28), and $\epsilon m_2 = m_{act}$ is the active torque. Explicitly one obtains

$$m_{act} = \frac{p_{act}}{\omega}\,,\; p_{act} = \frac{m_0}{H_0}f\,\frac{2\phi_c^5}{5}V_{cut}\,. \tag{46}$$

Here p_{act} is the power injected by NA operation. The active torque is positive (since $B_{pl} < H_0$), it is proportional to V_{cut} and has a $1/\omega$ dependence, unlike the passive one which is linear in ω.

D. Discussion of rolling velocity and force-velocity relation

Let us now discuss the results obtained analytically. In the case of weak enzymatic activity, we can combine Eq. (28) for the dissipative torque and Eq. (46) for the active driving torque to the torque balance $m_{diss} + m_{act} = 0 = -\xi_{diss}\omega + p_{act}/\omega$. This immediately implies a pitchfork bifurcation for the steady-state rolling velocity

$$\omega = \pm\sqrt{\frac{p_{act}}{\xi_{diss}}} \propto \phi_c\sqrt{f}\,\frac{\sqrt{\alpha V_{cut}}}{B_{pl}}\,. \tag{47}$$

This is exactly what had been observed in Fig. 3a), the velocity scaling like $\omega \propto \pm\sqrt{\beta}$ with $\beta \propto V_{cut}$ with V_{cut} linear in the NA concentration. As the total torque is zero, the torque scale $m_0 = \frac{1}{2}SR^2\rho_{HA}$ cancels out. Nevertheless the parameters S (linker stiffness) and R (radius of the virus) are still present since they enter the contact interval size ϕ_c. The result in fact depends on all model parameters, especially the kinetics of attachment/detachment and cutting contained in f.

Using the specific parameter values for influenza given in section II A, Eq. (47) yields values of the order of $\omega = 0.4\,\mathrm{s}^{-1}$. This compares well to the experimentally measured values by Sakai et al. [4, 5]: there, translational speeds of of $v \simeq 10 - 30\,\mathrm{nm/s}$ were reported, corresponding to ω between $0.2 - 0.6\,\mathrm{s}^{-1}$ for physiological NA activity.

To critically discuss the torque-angular velocity relation, we will introduce

$$A = \frac{\beta}{\alpha}, \tag{48}$$

which is an "activity parameter" proportional to the enzymatic activity. Adding now a term $5A\tilde{\omega}$ to Eq. (38), which represents a small correction since $\beta \ll \alpha$, allows us to combine the two obtained limits, Eq. (38) and Eq. (39) to one continuous curve,

$$\tilde{m}(\tilde{\omega}) \approx -\begin{cases}\tilde{\omega}\cdot\left(-4\tilde{\omega}^3 + 10\tilde{\omega}^2 - 10\tilde{\omega} + 5\left(1-A\right)\right) & ;\,\tilde{\omega}\leq 1\\ \tilde{\omega}^{-1} - 5A\tilde{\omega} & ;\,\tilde{\omega} > 1\end{cases} \tag{49}$$

where in addition we non-dimensionalized the torque $\tilde{m} = \frac{m}{m_c}$ with $m_c = m_0\frac{B_{pl}}{H_0}\frac{\phi_c^4}{5}$. Note that, maybe counterintuitively, the activity is now in front of the passive torque for the branch $\tilde{\omega} > 1$. This is due to the characteristic frequency, $\omega_0 = \frac{2\phi_c}{t_0} = \frac{2\phi_c}{t_m}A$, being proportional to the activity parameter: the higher the activity, the larger the rolling frequency must be to prevent the depletion zone at the back (the $B = 0$ region) to occur, and to stay in the regime $\tilde{\omega} > 1$.

Fig. 5 shows the torque-velocity relation from a numerical solution of the continuum model (red curve) as explained in section III B, and the approximate multi-line theory (green curve). The stochastic simulation results (symbols) shown additionally are explained in the next section. In view of the approximations made, the green curve given by Eq. (49) captures the behavior well on the semi-quantitative level and displays the same features as the numerically obtained red curve, namely three characteristic points:

(P_1): for $(\omega, m) = (0, 0)$ the virus is in the immobile state, which always should be a solution. (P_2): the point $(\omega, m) \approx \left(\frac{\sqrt{5}}{2}\omega_0, (5.6\,A - 0.8)\,m_c\right)$ characterizes the maximum sustainable torque (in the deterministic, mean-field model). For counter torques of larger amplitude, the motion is no longer stable. And finally (P_3): for $(\omega, m) = \left(\frac{\omega_0}{\sqrt{5A}}, 0\right) \propto \left(A^{1/2}, 0\right)$ the system is in the

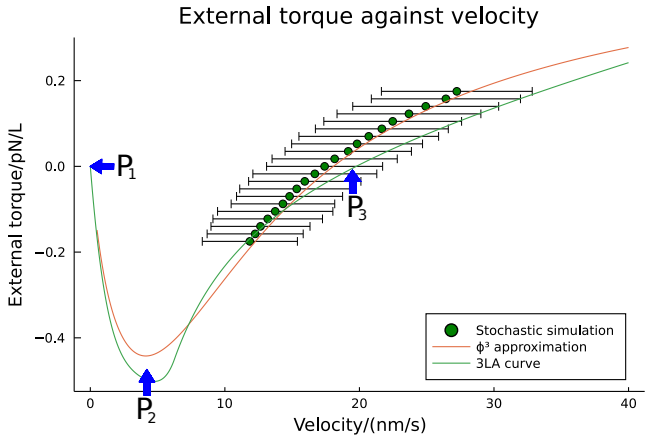


FIG. 5. Torque-velocity relation obtained from the numerical solution of the continuum model (red curve), from the approximate multi-line theory, Eq. (49), with β from the perturbation theory (green curve), and from stochastic simulations (symbols). Close to steady torque-free rolling, the agreement between numerics and stochastic simulations is excellent; the approximate theory displays the correct overall shape. The torque is given in pN/L where L is the virus' length along the cylinder axis. For the stochastic simulations, the velocity has been averaged over the whole simulated trajectory with error bars displaying standard deviation. The points P_1, P_2, P_3 characterizing the "motor curve" are discussed in the text.

steady, self-propelled rolling state and torque free, a behavior that is well captured already by Eq. (47).

Concerning (P_2), interestingly for small activity $A \to 0$ the maximum torque the virus can sustain becomes independent of the activity parameter: $m \to -0.8 m_c$. The corresponding minimal speed under subcritical forcing vanishes linearly with activity as $\omega = \frac{\sqrt{5}}{2}\omega_0 \propto A \to 0$. In the same (singular) limit, $A \to 0^+$, the torque-free motion, i.e. point (P_3), has no threshold and scales as $\omega_{free} \propto A^{1/2} \propto \phi_c\sqrt{\alpha V_{cut}}$, as already derived previously. Thus, in the absence of external torque and for arbitrary low activity A, one always has an (arbitrary slow) self-sustained rolling motion.

V. STOCHASTIC SIMULATIONS

A. Implementation and comparison stochastic vs. continuum model

So far we investigated the problem of rolling on the mean-field level, where we could show the existence of a steady rolling state for a virus having enzymatic NA activity. The questions whether this state is stable in view of the strongly fluctuating conditions at the nano scale and how the virus actually reaches this state, i.e. self-polarizes, demand a stochastic modeling framework. We here briefly explain the implementation of the model using the Gillespie algorithm (with details given in appendix C) and then critically compare the stochastic simulations to the continuum theory.

Let us consider a cylindrical virus, cf. Fig. 1, of length L and presenting a number of $N_{vir} \propto L$ discrete binding sites and project the cylinder onto a single cross-section. Then all binding sites (that one can assume randomly densely packed along the virus surface) get projected onto this circle. As the contact zone size, $2\phi_c R$ is fixed, the relation $N_{vir}\Delta x = 2\phi_c R$ defines the effective size Δx of a projected binding site. $N_{vir} \to \infty$ (i.e. $\Delta x \to 0$) represents the continuum deterministic limit. In turn, small N_{vir} can be interpreted as a circular virus, for which, using the size of an HA and a circular contact area, one estimates $N_{vir} \simeq 20$.

In the numerical algorithm, space is discretized by Δx on a large box (having typically $N = 2000 \gg N_{vir}$ sites) with periodic boundary conditions. The angular variable used in the mean field model is discretized accordingly, i.e. by $\phi = 2\phi_c n/N_{vir}$ defining the discrete bound linkers and free glycans, $B = B[n]$ and $G = G[n]$, respectively. To obtain the effective molar concentrations of the spike proteins and the ligands one needs to convert from known surface densities on the virus and the substrate to volume densities. Estimating the charateristic volume of a molecule by $V_m \sim (10\,\mathrm{nm})^3$, the molar concentration is given by $C_M = \frac{1l}{N_A V_m} \simeq 1\,\mathrm{mM}$, or in other words, 1 molecule/V_m corresponds to $\simeq 1\,\mathrm{mM}$.

The Gillespie method [26] is an event-driven algorithm, and time $t_i = \sum_{m=1}^{i} \Delta t_m$ is discretized in waiting times Δt_m. For every waiting time Δt_m one considers all possible events, i.e. binding, unbinding and cutting with their discretized rates. The waiting times are drawn according to $\Delta t_m = -\frac{\ln \xi}{a_T}$ where $\xi \in [0, 1]$ is a uniform random variable and a_T is the sum of the rates of all possible events (see appendix C for details). A second random number is used to choose which event takes place.

Finally, one has to evaluate the torque balance using the newly obtained linker configuration to determine the new center of mass position of the virus, $s(t_{i+1})$. Torque balance is assumed to be instantaneously established and, expressing the contact interval $[-\phi_c, \phi_c]$ via the binding sites $[n_L, n_R]$, the discretized torque balance reads

$$\sum_{n=n_L}^{n_R} (n - s)^3 \; B[n] = 0. \tag{50}$$

This is a cubic equation for $s = s(t_{i+1})$ (for details see appendix C) and always has a real solution that can be determined by root finding after every event that changes $B[n]$. Having the new position s (the nearest binding site is chosen), we get the new binding interval by shifting B to its new center of mass position s. This simulation yields trajectories $s(t_i)$, from which angular velocities $\omega(t_i)$ and velocities $v(t_i) = R\omega(t_i)$ can be readily determined, as well as the profiles $B[n], G[n]$ at every t_i.

To compare the stochastic implementation to the mean-field, continuum model we first choose a high number of linkers, $N_{vir} = 200$, such that effects like stochastic reversals of the direction of motion or even complete

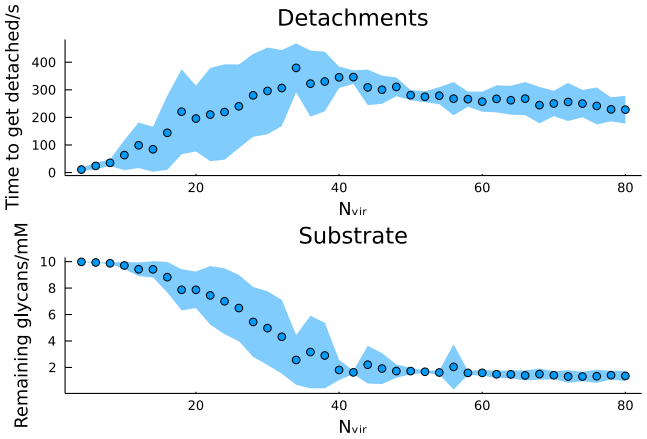


FIG. 6. Study of a virus (radius 50 nm, N_{vir} binding sites) rolling on a substrate with periodic boundary conditions (total number of binding sites 2000). Panel a) shows the average time until the virus detaches completely from the substrate as a function of the number of linkers N_{vir}. Panel b) shows the average glycan remaining on the substrate after the virus has detached, again as a function of the number of linkers. Averages were taken over 20 realizations for every value of N_{vir}, shaded areas show the standard deviation.

detachment of the virus do not occur (see next section for a discussion of these effects). If not stated otherwise, we simulate the system for the parameters, already given and discussed in section II. Going back to Fig. 5 that compares the torque-velocity relation obtained from stochastic simulations (symbols) to those from the numerical solution (red curve) and the approximate multiline theory (green curve) of the mean-field model, one can see that the numerics and the stochastic simulations agree very well in a substantial region around the torque-free rolling.

Interestingly, in the stochastic simulations we were unable to get the full branch from the torque-free rolling down to the minimum of $m(\omega)$: the virus always reverted its direction for large counter-torque, i.e. the system jumped to the negative velocity branch – note that for negative velocity, the torque velocity is the same curve as displayed for positive velocities, but upside-down. Without stochasticity, one would expect the branch to be stable down to the minimum and only the branch from the minmum up to $(m, \omega) = (0, 0)$ to be unstable. The latter branch corresponds to bound linker distributions with a three-line profile, i.e. where the glycan is completely cut at the back. This suggests that these states/profiles are important to understand the full torque-angular velocity relation, but that they are dynamically unstable, especially in the presence of stochastic fluctuations.

B. Stochastic effects: virus detachments and reversals

The stochastic implementation in addition allows to investigate the effects of finite linker numbers on the overall behavior of virus rolling, inducing for instance reversal of rolling direction or even complete detachment. Decreasing N_{vir} to values below 100 (for the given, realistic parameters), Fig. 6a) shows the time it takes for a virus, initially placed on a homogeneous glycan-covered substrate, to get completely detached – i.e. reaching the state with $B[n] = 0$ for all n in the contact zone. In turn, Fig. 6b) shows the averaged amount of glycan that is still left on the substrate, after the virus has detached.

Fig. 6 suggests that the origin of detachment for small values of N_{vir} is due to intrinsic stochasticity of binding, as the glycan level after detachment is still high. In contrast, for large values of N_{vir} the virus rather detaches since the glycan level becomes low. The latter is due to the fact that the virus consumes part of the substrate while rolling. It may also change direction of movement or go through the periodic box such that it crosses again the same, already partially glycan-depleted region more than once.

If the substrate were not consumed one would expect the time to get detached to grow exponentially with the number of linkers, since so does the number of possible configurations of $B[n]$. In order to study reversals and run times in a way that is not influenced by the history of the virus' path, in the following we will consider the case were the glycans are recovered by the cell. For simplicity we assume this recovery to be infinitely fast. Specifically, whenever a virus has rolled over a part of the substrate, the respective value $G(n)$ is restored to the initial level G_0. This corresponds to a virus rolling on a cell that has a high membrane diffusivity and rapidly reshuffles its surface glycans. We also come back to this point in section VII; note that glycan reshuffling via lateral diffusion within the cell membrane has been readily observed in experiments [27, 28].

Implementing this infinitely fast glycan recovery outside of the contact zone of the virus one can study the statistitics of the reversals of direction of the rolling virus and quantify the typical runlengths as a function of parameters and independent of the simulation box size. The results are shown in Fig. 7. The blue data in Panel a) show the frequency of reversals as a function of the number of linkers for homogeneous glycan distribution G_0 outside the contact zone. For the red data, we added a stochastic glycan distribution (noise level 50% of mean value). In both cases, the reversals decrease if the linker number increases. For the blue data, these reversals are solely due to the intrinsic stochasticity of the dynamics. As expected, for the noisy glycan distribution, reversals occur more frequently, but the rolling is still robust.

Fig. 7b) shows the average runlengths, i.e. the distance traveled between two reversals, obtained from the same raw data. The runlength increases with the number of

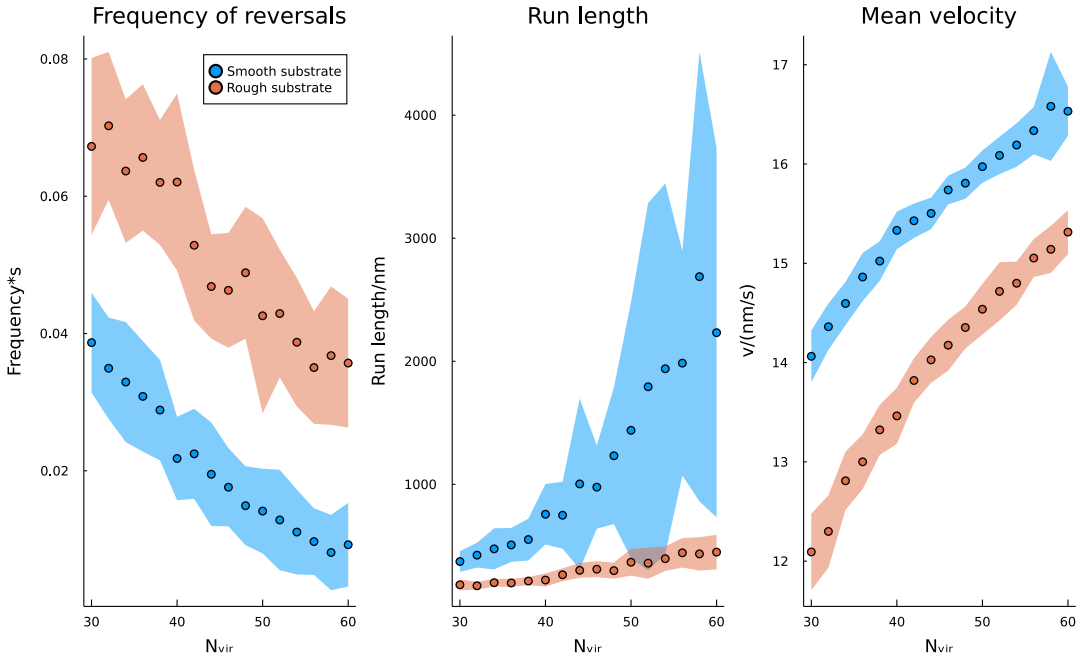


FIG. 7. Study of a virus (radius 50 nm, N_{vir} binding sites) rolling on a substrate with periodic boundary conditions (total number of binding sites 2000) and infinitely rapid glycan recovery outside the virus' contact zone. Panel a) shows the frequency of reversals (number per time) and panel b) the average run length between two reversals. Panel c) gives the average velocity obtained from the two former quantities. For the blue data the glycan distribution on the substrate was perfectly homogeneous at the standard value used, $G_0 = 10$, while for the red data a noisy distribution was implemented (with strong noise amplitude of $G_0/2$). All averages were taken over 20 runs of 500 s running time each, shaded areas show the standard deviation.

linkers and can easily reach several microns (meaning many tens the virus diameters) for a homogeneous glycan distribution. Noisy glycan distributions impede this substantially, but the virus still travels few times its size for still moderate linker numbers. Finally, from panels a) and b) one can estimate the mean velocity of the virus as shown in Fig. 7c). This is in good qualitative agreement with the theory/continuum model, which for the given parameters (and $N_{vir} \to \infty$) is 20 nm/s, cf. section IV D.

VI. FURTHER TOPICS

A. Approximations made, especially detailed balance for on-off kinetics

Within the simple model approach it is very satisfying to see the good agreement between the numerical and analytical approaches to the mean field model and the stochastic implementation. However, to be amenable to an analytical treatment, we made several – in part strong – approximations that should be critically discussed.

First, in section II C concerning the torque balance, we applied a small angle approximation for the contact angle. We checked numerically that for the given, realistic parameters, this has only a minor quantitative effect. Second, we neglected the effect of linker compression. In small angle approximation, linker compression can be included even analytically, with details given in appendix B. Again, this only leads to a quantitative correction.

The most critical approximation was made in section II D: namely, the simple model only approximately fulfills detailed balance for the HA-glycan on-off kinetics. In fact, while in section II B we used the force-dependence (and hence angle-dependence) of the attachment/detachment kinetics of the linkers to determine the size of the contact interval, this dependence was neglected in the dynamic equations, Eqs. (7), (8).

To improve on this point we now assume that the dissociation constant increases with the "Boltzmann factor" of the elastic stretch energy

$$\frac{K_d(\phi)}{K_d(0)} = \exp\left(\frac{E_{el}}{k_B T}\right) = \exp\left(\frac{SR^2}{8k_B T}\phi^4\right). \quad (51)$$

The equilibrium probablity distribution of the bound linkers is then given by $B_{pl}(\phi) = \frac{C_0 - C_1}{2}$, as given in section IV A, but now with the angle-dependent K_d entering C_0, C_1, explicitly

$$\frac{B_{eq}(\phi)}{H_0} = \frac{1}{2}\left(\bar{B} - \sqrt{\bar{B}^2 - 4\frac{G_0}{H_0}}\right) \quad (52)$$

with $\bar{B} = 1 + \frac{G_0 + K_d(\phi)}{H_0}$. The resulting $B_{eq}(\phi)$ implies a bell-shaped linker profile, with a maximum at $\phi = 0$ and decaying rapidly (like $\exp(-\phi^4)$) for finite angles.

We can now determine the size of the contact interval more properly: defining ϕ_c as the point where $p_{\text{bound}} =$

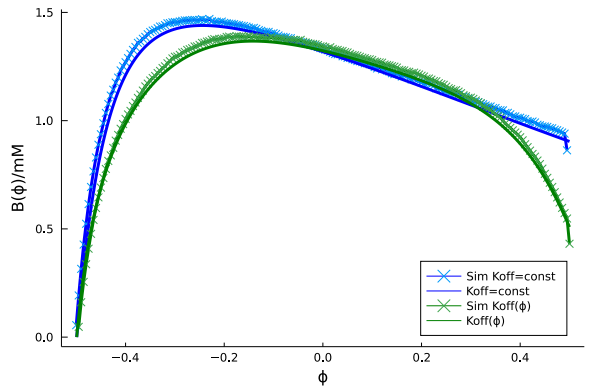


FIG. 8. Test of the effect of detailed balance of the on-off kinetics. Shown are bound linker distributions obtained numerically (solid) and by stochastic simulations (symbols). The blue curves are for the simple model (discussed throughout so far, without detailed balance), while the green curves obey detailed balance, i.e. $K_d(\phi)$ is angle-dependent as given by Eq. (51). In the latter case, the sloped linker profile in the center prevails and the virus is still able to roll steadily. Stochastic simulations are averaged over 10^6 realizations.

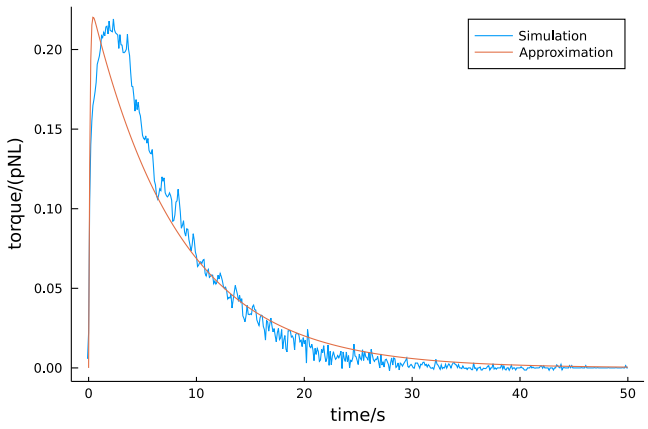


FIG. 9. Demonstration of the "mechano-chemical flywheel" effect. A virus that was rolling steadily was suddenly stopped at $t = 0$. Since the internal linker profile needs time to relax, a characteristic buildup of torque occurs with a characteristic time of the order of 10 s. Shown are results from stochastic simulations (blue; averaged over 10 events) and the scaling estimate, Eq. (53), in red (with no fitting parameter). Linker stiffness $S = 0.1 k_B T/\mathrm{nm}^2$, other parameters as given in section II.

$\frac{B_{eq}(\phi)}{H_0}$ drops below 1/2, from Eq. (52) one gets $G_0 - \frac{H_0}{2} = K_d(\phi_c)$. For typical parameters, $H_0/2 \ll G_0$ holds. Inserting Eq. (51) and solving for ϕ_c then yields exactly the scaling result, Eq. (3).

To scrutinize the effect of the detailed balance of the on-off kinetics on the bound linker distribution and ultimately on the rolling motion, we compared numerical solutions of the mean field model to stochastic simulations, both without detailed balance (constant K_d) and with detailed balance, i.e. $K_d(\phi)$. The result is shown in Fig. 8. The blue curve shows the case studied before, the two slopes quantified by α and β being clearly visible. The green curve shows the case with detailed balance. One can see that the bound linker profile decays much stronger both in rolling direction (to the left) and at the trailing edge (to the right), but overall the sloped distribution in the center region prevails and is sufficient to allow persistent rolling motion. We also checked that the speed is only quantitatively affected (for the given, realistic parameters by 10-20%).

B. Linker distribution as an "internal flywheel"

As observed already in Ref. [11], the Gillespie simulation-based computer experiments reveal a surprising robustness of the rolling virus: even when facing obstacles in form of glycan-depleted spots on the surface, the virus often just rolls over them as if it possesses an internal "inertia". A once directionally polarized virus can even persistently roll against a glycan gradient as long as there is a sufficient amount of glycan left to bind. Thus the virus is not performing a (chemo)taxis on the glycan concentration (as one would expect for a burned bridge Brownian ratchet). Instead the glycan acts here as a mechano-chemical free-energy source in analogy to the role of ATP for classical molecular motors. The fact that the glycan is confined (or sometimes even immobilized) on a 2D surface while ATP typically freely diffuses in 3D is only a superficial difference.

To understand the origin of the observed processivity behavior , we pose the following question: What happens when a steady rolling virus at initial angular velocity ω_{free} is suddenly stopped – by an external force, such as an immovable obstacle – at time $t = 0$? How does its torque $m(t)$ dynamically respond to this sudden constraint?

Initially, for $t < 0$, the virus was rolling in a torque-free state, implying that any torque buildup starts from $m(0) = 0$. The virus being blocked for $t > 0$, the advective (rolling) term is now missing in Eqs. (7), (8) and the linker distribution in the front region will respond by rapidly equilibrating to the plateau-value there. This front equilibration has the timscale $t \sim B_{pl}/\alpha$ and due to torque imbalance it is accompanied by an buildup of torque $m(t)$. While the front region's slope (cf. Fig. 2) becomes flatter during this fast and transient process, the more extended, cutting-dominated rear region stays roughly unperturbed as it responds much slower. This implies a maximum torque $m_{max} \propto -\beta/\omega_{free}$ given only by the cutting-induced gradient at the rear. Finally, on the long timescale $t \sim B_{pl}/\beta$, the progressive NA linker-cutting makes the linker profile decay to zero in the whole contact zone, leading to a gradually vanishing torque $m(t) \to 0$. In summary, a suddenly stopped virus responds with a transient torque buildup for $t > 0$ of the

approximate form

$$m(t) \simeq m_{max} \tanh\left(\frac{\alpha}{B_{pl}}t\right) e^{-\frac{\beta}{B_{pl}}t} \tag{53}$$

where $m_{max} \simeq p_{act}/\omega_{free}$.

Figure 9 shows a comparison of the torque buildup measured in stochastic simulations (averaged over 10 stopping events) and the scaling formula, Eq. (53). It confirms the interpretation that a stopped virus mobilizes its bound linkers and puts up dynamic resistance against the obstacle. One could say that the system formally behaves as if it possessed a built-in "flywheel" – here of mechano-chemical origin – that is dissipatively coupled to the rolling angle variable and tends to maintain its angular momentum. This "flywheel" dynamic response is associated to the re-equilibration of an internal nonequilibrium steady state. It seems to be a defining feature of other dissipative rolling objects as well [35, 36, 45] and deserves closer inspection in the future.

VII. DISCUSSION

We have proposed and analyzed a new mechanism allowing a virus to actively roll along a substrate and shown that this rolling is essentially inevitable, once few basic conditions are met: namely, (1) existence of a rolling axis for the virus, (2) presence of ligands on the substrate, and (3) viral spikes (one or several types) that bind *and* enzymatically cut these ligands. The obvious question to ask next is: how does the virus benefit from it?

Why the rolling?

Obviously, being a nanoscale object the virus could just move through the bulk of a low viscosity fluid via thermal diffusion. However, in the case of mucus-binding viruses like influenza, the large viscosity and the gel-like nature of the environment severely limits this. An additional danger influenza faces is getting stuck in/to the mucus and eventually being swept away by the beating cilia of our respiratory tract. To make the situation even worse for the virus, during its entry phase [29, 30] the virus can become localized at wrong spots on the cell membrane (or on a wrong cellular structure like a cilium), being unable to enter the cell at all. If the cell membrane is sufficiently fluid, two-dimensional (2D) diffusion can help out, but not if the glycan receptors (glycolipids and proteins) are trapped within local membrane domains controlled by the cytoskeleton underneath. Influenza could respond by weakening its bonds with the immobile glycans in order to still diffuse on the quasi-rigid substrate, the drawback being that increasing diffusivity also increases the virus-membrane detachment rate. All these are likely reasons for influenza having evolutionary come up with the active enzyme solution.

In spite of sufficiently strong collective, multi-linker binding by the HA-spikes, the virus can still actively weaken these links via the NA-spikes' cutting activity. However, if this form of "stick-and-cut" behavior was spatially uncoordinated, it would be difficult to comprehend how it could give rise to any sufficiently fast or even directed motion. How should the virus decide which way to go and keep a certain persistence of direction? Obviously, the (immobile) glycan-covered substrate could help the virus to some extent by keeping records of where the virus has already been: the virus would then simply statistically avoid the NA-generated glycan-depleted regions and perform a form of 2D self-avoiding walk, which is the idea underlying the so-called burnt-bridge Brownian ratchet [9, 10]. This strategy could be enhanced by a polarized distribution of the spikes [20], with NA enriched at the rear, depleting more glycans there, and HA enriched in front, both effects enhancing forward binding and stabilizing directional movement. Indeed this is observed for IVA where HA and NA are physically separated molecules "floating" rather freely in the membrane, where they can polarize the virus via a partial phase separation. The motion in this case happens *along the long axis* of the ellipsoidal or filamentous virus. However, for IVC the two spikes are "glued together" into a single, inseparable unit, the HEF protein [19]. Naively, this additional constraint would make the virus less motile, yet the opposite is true: IVC moves about 5-10 times faster than IVA [4, 5]. In addition to its larger speed, most notably IVC moves *orthogonally to its long axis*.

It seems that these two propulsion modes – parallel and orthogonal to the axis – have radically different physical mechanisms. Here we suggested that the motion orthogonal to the cylindrical axis is tightly coupled to axial rotation. This coupling is more than just an easy, low dissipation mode of motion, but rather intrinsically linked to the very mechanism of dynamic linker polarization: on the one hand, the angular rotation itself leads to a linker polarization within the virus-substrate contact zone. On the other hand, the linker polarization front vs. rear gives rise to a torque and the angular velocity. Both interdependent effects are inseparable and make rolling propulsion fast, robust and efficient compared to longitudinal gliding.

The emergence of rolling can be seen as a step in the evolutionary race between the virus and the host. Naturally, this race is still ongoing and the host could also take counter measures. One possibility is the mixing-up and quick replacement of the cut glycans by fresh ones (cf. the glycan recovery in section V B). However, for this to be efficient it has to affect the contact zone, as the rolling virus is not very sensitive to gradients outside. Hence glycan replacement must be extremely fast (the virus passes the contact zone within few seconds). Another possibilty is to "clog" the rotation by firmly binding ligands (antibodies) to some of the free HA/HEF. In this case, the virus would have to resort to other, less efficient propulsion mechanisms like gliding. Alternatively, it could counter-

act the clogging by allowing sterically blocked HA/HEF to float by keeping the transmembrane proteins (including the spikes) in a fluid state. As just sketched here, the game-theory of this intricate evolutionary race promises new surprises for future studies.

Experimental Questions

From the experimental point of view, advancing elegant in vitro setups like those by Sakai et al. [4, 5] should allow to quantitatively probe the detailed mechanism proposed here, the most robust and easy-to-test predictions being:
(1) The rolling speed as a function of NA, HA, and glycan surface-concentrations. Especially the characteristic square root relation $\omega \propto \sqrt{V_{cut}}$, cf. Eq. (47), between the angular velocity and the cutting rate $V_{cut} \propto [NA]$.
(2) The force-velocity or "motor relation" shown in Fig. 5 and the characteristic points P_1-P_3 therein, as well as the scaling behavior of the curve.
(3) The instantaneous force response of a stalled, immobilized virus, as shown in Fig. 9 and quantified in Eq. (53).

Experimentally these should be accessible as the filamentous viruses are large (long axis one micron) and sufficiently slow (tens of nm/s) to be readily captured by various microscopy methods. Even smaller viruses have been studied already using high resolution techniques [31]. The force magnitudes (tens of pN) and their moderately slow time evolution (few seconds) are also well within the range of common force spectroscopy methods [32, 33]. To test the theory it is most practical to utilize filamentous viruses. Although the model developed here also applies to spherical viruses on small time scales, the high rotational diffusion constant of a tiny nanosphere and the small number of linkers making contact ($N_{vir} \simeq 20$) will in this case give rise to large orientational and velocity fluctuations. As for any directionally self-propelled object of characteristic size L, there will be a crossover from ballistic to diffusive motion at a timescale $t_{rot} \propto 1/D_{rot}$ with $D_{rot} \propto L^{-3}$ the rotational diffusion constant. While for a sphere L will be the radius, for a cylinder it will be its length, making the directed propulsion of the latter experimentally much easier to probe.

Many interesting questions still remain, including the role of the different motility modes – gliding by spike polarization [20] and rolling [4, 5] – under similar conditions. Can IVA actually switch between the two motility modes? And how do IVs finally switch from rolling to entering the cell [29, 30, 34]?

On the physics side there is an interesting conceptual question that still needs to be addressed: Other non-equilibrium filamentous rollers are known to exist, but these are bulk-driven, meaning there is a matter-energy flow (e.g. of heat [35] or solvent [36]) through the cross-section of the cylinder. So what are similarities and differences of active rollers that are bulk-driven vs. surface-driven in view of a general description, their efficiency, or the existence and nature of their internal flywheel modes?

VIII. CONCLUSIONS

In conclusion, the rolling mechanism renders influenza an even smarter adversary than previously thought. In contrast to classical virology dogmas, this virus type displays a "surface metabolism" harvesting the chemical energy of sugars on the host's membrane for directional force generation. In turn, this transforms the whole virus capsid into a complex rotary motor. The underlying linker dynamics shares similarities with passive (e.g. shear induced [37–39]) or other [40] adhesive rolling mechanisms, as well as with collective motor ensembles [41–43], but with the crucial addition of the enzymatic substrate cutting. The mechanism discussed here for influenza should also apply to other viruses having enzymatic spike proteins: candidates are the toro-virus and some of the beta-corona-viruses [44]. We can also flip the coin and learn from the virus' workings: in fact, the combination of a binding molecule, a cutting enzyme and the spherical/cylindrical geometry has been already used to propel DNA-coated beads [45–47] along RNA-covered surfaces and the insights developed here could now be used to optimize such and related artificial rollers.

IX. APPENDIX

Appendix A: Calculation in angle space and scaling

The calculation of the torque becomes especially transparent in angle space, where the two-line linker distribution reads

$$B(\phi) = \begin{cases} \frac{\alpha}{\omega}(\phi + \phi_c) & \text{for } -\phi_c \le \phi \le \phi_{pl} \\ \frac{\alpha}{\omega}(\phi_{pl} + \phi_c) - \frac{\beta}{\omega}(\phi - \phi_{pl}) & \text{for } \phi_{pl} \le \phi \le \phi_c \end{cases} \tag{A1}$$

Rewriting the torque, Eq. (4), by again using that a constant linker distribution is torque-free, yields

$$m = -\frac{m_0}{H_0}\frac{1}{\omega}\left[\alpha\int_{-\phi_c}^{\phi_{pl}}(\phi - \phi_{pl})\phi^3 d\phi - \beta\int_{\phi_{pl}}^{\phi_c}(\phi - \phi_{pl})\phi^3 d\phi\right] \tag{A2}$$

In the first integral, one substitutes $\tilde{\phi} = \phi + \phi_c$ and uses that $\phi_{pl} + \phi_c \ll 1$. In the second one uses $\phi_{pl} \simeq -\phi_c$. Both amount to the same statement, that the plateau is rapidly reached (i.e. closeby the boundary in rolling direction). One obtains

$$m = -\frac{m_0}{H_0}\left[\frac{\alpha}{\omega}\frac{1}{2}(\phi_{pl} + \phi_c)^2\phi_c^3 - \frac{\beta}{\omega}\frac{2}{5}\phi_c^5\right], \tag{A3}$$

and using $\phi_{pl} + \phi_c = \omega t_m$ one regains

$$m = -\frac{m_0}{H_0}\left[\alpha\omega\frac{1}{2}\left(t_m\right)^2\phi_c^3 - \frac{\beta}{\omega}\frac{2}{5}\phi_c^5\right]. \qquad \text{(A4)}$$

As stated already in section III A when discussing the scaling, if the plateau is reached sufficiently rapidly, the torque integral over the negative slope region is independent of the dynamics. Basically, there is degradation everywhere, resulting just in a power of ϕ_c, the contact area size. It only remains the $1/\omega$-dependence from the slope in angle space. In contrast, for the first, passive contribution, cf. Eq. (A3), the dynamics is important: the angle-integrated slope yields a square-dependence in the plateau angle and hence in ω, which together with the $1/\omega$ from the slope yields a linear friction $\propto \omega$.

Appendix B: Effect of linker compression

In section II C we introduced a distribution of linker extensions, that was assumed to be zero at the symmetry axis and growing quadratically with angle ϕ. This implied only tensile linker forces for $\phi \neq 0$ and a delta-peak counter-force with opposite sign at $\phi = 0$. Physically, this assumption means that the stiff viral spike proteins can sustain a compressive load with little compliance but they easily stretch when tension is applied.

One can take the concept of linear linker elasticity more seriously and allow the virus to push down on and compress the linkers. Assuming a similar chain stretching as before, including the possibility that the virus cross-section is shifted downwards by a (to be determined) length l_0, one has $l(\phi) = R(1-\cos(\phi)) - l_0$. The energy of the elastic spring foundation reads (for small ϕ)

$$e_{el}(\phi) = \frac{S}{2}l^2(\phi) \simeq \frac{SR^2}{2}\left(\phi^2/2 - \varepsilon_0\right)^2, \qquad \text{(B1)}$$

with $\varepsilon_0 = l_0/R$ the vertical deformation. It is determined to be $\varepsilon_0 = \frac{1}{6}\phi_c^2$ by the vanishing force condition, $\int_{-\phi_c}^{\phi_c} f_{el}(\phi)d\phi = 0$, with $f_{el} = -\frac{\partial e_{el}(\phi)}{\partial l}$. The torque balance, Eq. (4), then generalizes to

$$m_{\text{incl compr}} = -\frac{m_0}{H_0}\int_{-\phi_c}^{\phi_c} B(\phi)\left(\phi^3 - 2\varepsilon_0\phi\right)\,d\phi\,. \qquad \text{(B2)}$$

In addition to the third moment, there now also is a contribution from the first moment, having opposite sign. Evaluating this torque using Eq. (A1) leads to $\omega_{\text{incl compr}} = \sqrt{2/3}\,\omega$ implying a reduction of $\simeq 20\%$.

Appendix C: Details for the stochastic implementation

The Gillespie algorithm [26] is event driven: at any time step, one decides whether at the picked position n a binding event ($B[n] \to B[n]+1$ and $G[n] \to G[n]-1$), an unbinding event ($B[n] \to B[n]-1$ and $G[n] \to G[n]+1$) or a cutting event ($G[n] \to G[n]-1$) occurs. The weights of these events can be read off directly from Eqs. (7), (8):

$$a_b[n] = k_{on}G[n](H_0 - B[n])\,,\;\; a_u[n] = k_{off}B[n],$$
$$a_c[n] = V_{cut}\frac{G[n]}{G[n]+K_M}, \qquad \text{(C1)}$$

which must be normalized by the sum $a_T = \sum_n (a_b[n] + a_u[n] + a_c[n])$ to assign probabilities to each process. The waiting times Δt_m between two events can then be picked as $\Delta t_m = -\frac{\ln\xi}{a_T}$, with ξ a uniform random variable on $[0,1]$.

Finally, to find the new center of mass position of the virus, at each step one solves Eq. (50), i.e. the cubic equation,

$$s^3 + c_2 s^2 + c_1 s + c_0 = 0, \qquad \text{(C2)}$$

with coefficients determined by the bound linkers as

$$c_2 = -\frac{3}{\Sigma}\sum_{i=i_L}^{i_R} n\,B[n]\,,\;\; c_1 = \frac{3}{\Sigma}\sum_{i=i_L}^{i_R} n^2\,B[n]\,,$$
$$c_0 = -\frac{1}{\Sigma}\sum_{i=i_L}^{i_R} n^3\,B[n]\,, \qquad \text{(C3)}$$

where $\Sigma = \sum_{i=i_L}^{i_R} B[n]$.

[1] R. Dawkins, Why don't animals have wheels? Sunday Times, November 24 (1996).
[2] R. Alon, D. A. Hammer, and T. A. Springer, Nature **374**, 539 (1995).
[3] B. M. Cooke, A. R. Berendt, A. G. Craig, J. Macgregor, C. I. Newbold, et al. Br. J. Haematol. **87** 162 (1994)
[4] T. Sakai, S. I. Nishimura, T. Naito and M. Saito, Sci. Rep. **7**, 45043 (2017).
[5] T. Sakai, H. Takagi, Y. Muraki and M. Saito, J. Virol. **92**, e01522-17 (2018).
[6] H. Guo, H. Rabouw, A. Slomp, M. Dai, F. van der Vegt, et al., PLoS Pathog. **14**, e1007233 (2018).
[7] E. de Vries, W. Du, H. Guo and C.A.M. de Haan, Trends Microbiol. **28**, 57 (2020).
[8] N. J. Overeem, E. van der Vries and J. Huskens, Small **17**, 2007214 (2021).
[9] J. Mai, I. M. Sokolov and A. Blumen, Phys. Rev. E. **64**, 011102 (2001).
[10] T. Antal and P.L. Krapivsky, Phys. Rev. E. **72**, 046104 (2005).

[11] F. Ziebert and I. M. Kulić, Phys. Rev. Lett. **126**, 218101 (2021).
[12] P. Ball, Physics **14**, 82 (2021).
[13] M. D. Badham and J. S. Rossman, Curr. Clin. Microbiol. Rep. **3**, 155 (2016).
[14] B. Dadonaite, S. Vijayakrishnan, E. Fodor, D. Bhella and E. C. Hutchinson, J. Gen. Virol. **97**, 1755 (2016).
[15] J. N. Varghese, W. G. Laver, P. M. Colman, Nature **303**, 35 (1983).
[16] D.C. Wiley and J.J. Skehel, Annu. Rev. Biochem. **56**, 365 (1987).
[17] S. J. Gamblin and J. J. Skehel, J. Biol. Chem. **285**, 28403 (2010).
[18] D. Dou, R. Revol, H. Östbye, H. Wang and R. Daniels, Front. Immunol. **9**, 1581 (2018).
[19] M. Wang and M. Veit, Protein Cell **7**, 28 (2016).
[20] M. D. Vahey and D. A. Fletcher, eLife **8**, e43764 (2019).
[21] N. K. Sauter, M. D. Bednarski, B. A. Wurzburg, J. E. Hanson, G. M. Whitesides, et al., Biochem. **28**, 8388 (1989).
[22] N. K. Sauter, J. E. Hanson, G. D. Glick, J. H. Brown, R. L. Crowther, et al., Biochem. **31**, 9609 (1992).
[23] S. E. Adams, N. Lee, V. Y.Lugovtsev, A. Kan, R. P. Donnelly and N. A. Ilyushina, Antiviral Res. **169**, 104539 (2019).
[24] E. Evans and K. Ritchie, Biophys. J. **72**, 1541 (1997).
[25] As a side note, avoiding the adiabatic approximations used above one still gets after a lengthy calculation a very similar result, but with f replaced by

$$f_{na} = \frac{H_0 - B_{pl}}{K_d + G_{pl} + H_0 - B_{pl}} \frac{G_{pl}}{K_M + G_{pl}}.$$

Using typical parameter values (see section II), this differs from the above only by few percents.
[26] D. T. Gillespie, J. Phys. Chem. **81**, 2340 (1977).
[27] X. Zhou, M. Zhao, Y. Liu, Q. Chen, and L. Shen, Langmuir 36, 15212 (2020)
[28] H. Jiang, B.P. English, R.B. Hazan, P. Wu and B. Ovryn Angew. Chem. Int. Ed., 54, 1765 (2015)
[29] S. Boulant, M. Stanifer and P.-Y. Lozach, Viruses, **7**, 2794 (2015).
[30] M. Koehler, M. Delguste, C. Sieben, L. Gillet and D. Alsteens, Annu. Rev. Virol. **7**, 143 (2020).
[31] P. Kukura, H. Ewers, C. Müller, A. Renn, A. Helenius, and V. Sandoghdar, Nat. Methods, **6**, 923 (2009).
[32] M. Müller, D. Lauster, H. H. K. Wildenauer, A. Herrmann and S. Block, Nano Lett. **19**, 1875 (2019).
[33] J. L. Cuellar-Camacho, S. Bhatia, V. Reiter-Scherer, D. Lauster, S. Liese, J. P. Rabe, A. Herrmann and R. Haag, J. Am. Chem. Soc. **142**, 12181 (2020).
[34] R. Du, Q. Cui and L. Rong, Viruses **11**, 458 (2019).
[35] A. Baumann, A. Sánchez-Ferrer, L. Jacomine, P. Martinoty, V. Le Houerou, F. Ziebert and I. M. Kulić, Nat. Mater. **17**, 523 (2018).
[36] A. Bazir, A. Baumann, F. Ziebert and I. M. Kulić, Soft Matter **16** 5210 (2020).
[37] E. F. Krasik and D. A. Hammer, Biophys. J. **87**, 2919 (2004).
[38] C. B. Korn and U. S. Schwarz, Phys. Rev. E **77**, 041904 (2008).
[39] A. K. Dasanna, D. A. Fedosov, G. Gompper, and U. S. Schwarz, Soft Matter **15**, 5511 (2019).
[40] C. S. Korosec, L. Jindal, M. Schneider, I. Calderon de la Barca, M. J. Zuckermann, N. R. Forde and E. Emberly, Soft Matter **17**, 1468 (2021).
[41] F. Jülicher and J. Prost, Phys. Rev. Lett. **75**, 2618 (1995).
[42] F. Jülicher, A. Ajdari, and J. Prost, Rev. Mod. Phys. **69**, 1269 (1997).
[43] P. Reimann, Phys. Rep. **361**, 57 (2002).
[44] R.J. de Groot, Glycoconj. J. **23**, 59 (2006).
[45] K. Yehl, A. Mugler, S. Vivek, Y. Liu, Y. Zhang, et al., Nat. Nanotechnol. **11**, 184 (2016).
[46] A. T. Blanchard, A. S. Bazrafshan, J. Yi, J. T. Eisman, K. M. Yehl, et al., Nano Lett. **19**, 6977 (2019).
[47] A. Bazrafshan, T. A. Meyer, H. Su, J. M. Brockman, A. T. Blanchard, et al., Angew. Chem. Int. Ed. **59** 2 (2020).